Unsteady Transonic Algorithm Improvements for Realistic Aircraft Applications

John T. Batina*
NASA Langley Research Center, Hampton, Virginia

Improvements to a time-accurate approximate factorization (AF) algorithm have been implemented for steady and unsteady transonic analysis of realistic aircraft configurations. These algorithm improvements have been made to the Computational Aeroelasticity Program—Transonic Small Disturbance (CAP-TSD) code developed recently at NASA Langley Research Center. The code permits the aeroelastic analysis of complete aircraft in the flutter critical transonic speed range. The AF algorithm of the CAP-TSD code solves the unsteady transonic small-disturbance equation. The algorithm improvements include an Engquist-Osher (E-O) type-dependent switch to more accurately and efficiently treat regions of supersonic flow, extension of the E-O switch for second-order spatial accuracy in these regions, nonreflecting far-field boundary conditions for more accurate unsteady applications, and several modifications that accelerate convergence to steady state. Calculations are presented for several configurations including the General Dynamics one-ninth scale F-16C aircraft model to evaluate the algorithm modifications. The modifications have significantly improved the stability of the AF algorithm and, hence, the reliability of the CAP-TSD code in general. The paper presents detailed descriptions of the algorithm improvements along with results and comparisons that demonstrate the improved stability, accuracy, and efficiency of the CAP-TSD code.

Nomenclature

c = airfoil chord
$c_{l\alpha}$ = unsteady lift-curve slope
c_r = wing reference chord
C_p = pressure coefficient
k = reduced frequency, $\omega c_r/2U$
M = freestream Mach number
R = residual
t = time, nondimensionalized by freestream speed and wing reference chord
u = sonic value of streamwise disturbance speed
U = freestream speed
α = instantaneous angle of attack
α_0, α_1 = mean angle of attack and amplitude of pitch oscillation
γ = ratio of specific heats
Δt = nondimensional time step
$\bar{\eta}$ = fractional semispan
ϕ = disturbance velocity potential
ω = angular frequency

Subscripts

t = tail
w = wing

Introduction

CURRENTLY, considerable research is being conducted to develop finite-difference computer codes for calculating transonic unsteady aerodynamics for aeroelastic applications.[1] These computer codes are being developed to provide accurate methods of calculating unsteady air loads for the prediction of aeroelastic phenomena such as flutter and divergence. For example, the CAP-TSD[2] unsteady transonic small-disturbance (TSD) code was recently developed for transonic aeroelastic analyses of complete aircraft configurations. The name CAP-TSD is an acronym for Computational Aeroelasticity Program—Transonic Small Disturbance. The new code permits the calculation of unsteady flows about complete aircraft for aeroelastic analysis in the flutter critical transonic speed range. The code can treat configurations with arbitrary combinations of lifting surfaces and bodies including canard, wing, tail, control surfaces, tip launchers, pylons, fuselage, stores, and nacelles. In Ref. 2, steady and unsteady pressures were presented for several complex aircraft configurations that demonstrated the geometrical applicability of CAP-TSD. These calculated results were in good agreement with available experimental pressure data that validated CAP-TSD for multiple component applications with mutual aerodynamic interference effects. Preliminary aeroelastic applications of CAP-TSD were presented in Ref. 3 for a simple well-defined wing case. The case was selected as a first step toward performing aeroelastic analyses for complete aircraft configurations. The calculated flutter boundaries compared well with the experimental data for subsonic and supersonic freestream Mach numbers, which gives confidence in CAP-TSD for aeroelastic prediction.

The CAP-TSD code uses a time-accurate approximate factorization (AF) algorithm recently developed by Batina[4] for solution of the unsteady TSD equation. The AF algorithm involves a Newton linearization procedure coupled with an internal iteration technique. In Ref. 4, the algorithm was shown to be efficient for application to steady or unsteady transonic flow problems. It can provide accurate solutions in only several hundred time steps, yielding a significant computational cost savings when compared to alternative methods. For reasons of practicality and affordability, an efficient algorithm and a fast computer code are requirements for realistic aircraft applications.

The purpose of this paper is to describe recent changes to the CAP-TSD code that have significantly improved the stability of the AF algorithm and the accuracy of the results. The algorithm modifications include 1) improved type-dependent differencing to treat regions of supersonic flow, 2)

Received Dec. 8, 1987; presented as Paper 88-0105 at the AIAA 26th Aerospace Sciences Meeting, Reno, NV, Jan. 11-14, 1988; revision received July 19, 1988.

*Research Scientist, Unsteady Aerodynamics Branch, Structural Dynamics Division. Senior Member AIAA.

extension of the type-dependent differencing for second-order spatial accuracy, 3) nonreflecting far-field boundary conditions for unsteady applications, and 4) several modifications to accelerate convergence to steady state. The paper presents detailed descriptions of these algorithm improvements along with results and comparisons that assess the improved stability, accuracy, and efficiency of the CAP-TSD code.

Algorithm Improvements

Engquist-Osher Type-Dependent Switch

Algorithms based on the TSD equation typically use central differencing in regions of subsonic flow and upwind differencing in regions of supersonic flow. This, of course, allows for the correct numerical description of the physical domain of dependence. The original CAP-TSD code of Ref. 2 used the Murman[5] type-dependent switch to change the spatial differencing. The Murman switch, however, admits nonphysical expansion shocks as a part of the solution and has been shown to be less stable than monotone methods.[6,7] For example, unsteady results for a NACA 64A006 airfoil were presented in Ref. 7, which demonstrated an order of magnitude increase in time step using a monotone algorithm. Therefore, an Engquist-Osher (E-O) monotone switch, similar to that of Ref. 6, has been incorporated within the AF algorithm of the CAP-TSD code. The E-O switch is based on sonic reference conditions and does not admit expansion shocks as part of the solution. Use of the E-O switch also generally increases computational efficiency because of the larger time steps that may be taken. Mathematical details of the required algorithm changes are described in a subsequent section.

Second-Order-Accurate Spatial Differencing

Most TSD algorithms are only first-order accurate spatially in regions of supersonic flow. This is due to the first-order upwind differencing that is typically used to treat these regions. Use of second-order upwind differencing has been shown to improve the accuracy of the solution while retaining the numerical stability of the first-order method.[8] Consequently, the E-O type-dependent switch of the AF algorithm has been extended for second-order spatial accuracy in supersonic regions of the flow. Comparisons of results obtained using first-order and second-order differencing, to be presented, demonstrate the improved accuracy of the second-order method.

Nonreflecting Far-Field Boundary Conditions

For unsteady applications, the far-field boundary conditions can have a significant influence on the accuracy of the solution. Steady-state boundary conditions are inadequate for unsteady calculations, since disturbances reaching the boundaries are reflected back into the computational domain. These reflected disturbances can propagate into the near field and, thus, produce inaccurate results. One solution to this problem is to locate the grid boundaries far away to minimize the effect of the boundary conditions. This is generally not an acceptable remedy because of the higher computational cost that results from an increased number of grid points required to discretize a larger computational domain. The more appropriate solution is the use of nonreflecting far-field boundary conditions which absorb most of the waves that are incident on the boundaries and, consequently, allow the use of smaller computational grids.[9] Nonreflecting boundary conditions similar to those of Whitlow[9] have been incorporated within the CAP-TSD code. These boundary conditions are consistent with the AF solution procedure and are described in more detail below. Results obtained with and without the nonreflecting boundary conditions are presented which demonstrate their effectiveness.

Steady-State Convergence Acceleration

Finally, several algorithm changes have been made to accelerate convergence to steady state. Besides the E-O switch, these changes include 1) deletion of the time-dependent terms from the residual of the AF algorithm, 2) deletion of all of the time derivatives of the TSD equation, and 3) overrelaxation of the residual. The effects of these modifications on the steady-state convergence are demonstrated in the results presented herein.

Transonic Small-Disturbance Equation

The flow is assumed to be governed by the general frequency modified TSD potential equation, which may be written in conservation law form as

$$\frac{\partial f_0}{\partial t} + \frac{\partial f_1}{\partial x} + \frac{\partial f_2}{\partial y} + \frac{\partial f_3}{\partial z} = 0 \tag{1}$$

where

$$f_0 = -A\phi_t - B\phi_x \tag{2a}$$

$$f_1 = E\phi_x + F\phi_x^2 + G\phi_y^2 \tag{2b}$$

$$f_2 = \phi_y + H\phi_x\phi_y \tag{2c}$$

$$f_3 = \phi_z \tag{2d}$$

The coefficients A, B, and E are defined as

$$A = M^2, \qquad B = 2M^2, \qquad E = 1 - M^2 \tag{3}$$

Several choices are available for the coefficients F, G, and H depending upon the assumptions used in deriving the TSD equation.[2] The coefficients are herein defined as

$$F = -(1/2)(\gamma + 1)M^2, \qquad G = (1/2)(\gamma - 3)M^2,$$

$$H = -(\gamma - 1)M^2 \tag{4}$$

Approximate Factorization Algorithm

An approximate factorization algorithm was developed[4] to solve the modified TSD equation [Eq. (1)]. In this section, the AF algorithm is described.

General Description

The AF algorithm consists of a Newton linearization procedure coupled with an internal iteration technique. For unsteady flow calculations, the solution procedure involves two steps. First, a time linearization step (described below) is performed to determine an estimate of the potential field. Second, internal iterations are performed to minimize linearization and factorization errors. Specifically, the TSD equation (1) is written in general form as

$$R(\phi^{n+1}) = 0 \tag{5}$$

where ϕ^{n+1} represents the unknown potential field at time level $(n + 1)$. The solution to Eq. (5) is then given by the Newton linearization of Eq. (5) about ϕ^*

$$R(\phi^*) + \left(\frac{\partial R}{\partial \phi}\right)_{\phi=\phi^*} \cdot \Delta\phi = 0 \tag{6}$$

In Eq. (6), ϕ^* is the currently available value of ϕ^{n+1}, and $\Delta\phi = \phi^{n+1} - \phi^*$. During convergence of the iteration procedure, $\Delta\phi$ will approach zero so that the solution will be given by $\phi^{n+1} = \phi^*$. In general, only one or two iterations are required to achieve acceptable convergence. For steady flow calculations, iterations are not used because time accuracy is not necessary when marching to steady state.

Mathematical Formulation

The AF algorithm is formulated by first approximating the time derivative terms (ϕ_{tt} and ϕ_{xt} terms) by second-order-accurate finite-difference formulae. The TSD equation is rewritten by substituting $\phi = \phi^* + \Delta\phi$ and neglecting squares of derivatives of $\Delta\phi$, which is equivalent to applying Eq. (6) term by term. The resulting equation is then rearranged, and the left-hand side is approximately factored into a triple product of operators yielding

$$L_\xi L_\eta L_\zeta \Delta\phi = -\sigma R(\phi^*, \phi^n, \phi^{n-1}, \phi^{n-2}) \tag{7}$$

where

$$L_\xi = 1 + \frac{3B}{4A}\xi_x \Delta t \frac{\partial}{\partial\xi} - \xi_x \frac{\Delta t^2}{2A}\frac{\partial}{\partial\xi} F_1 \frac{\partial}{\partial\xi} \tag{8a}$$

$$L_\eta = 1 - \xi_x \frac{\Delta t^2}{2A}\frac{\partial}{\partial\eta} F_2 \frac{\partial}{\partial\eta} \tag{8b}$$

$$L_\zeta = 1 - \xi_x \frac{\Delta t^2}{2A}\frac{\partial}{\partial\zeta} F_3 \frac{\partial}{\partial\zeta} \tag{8c}$$

$$F_1 = E\xi_x + 2F\xi_x^2\phi_\xi^* + 2G\xi_y(\xi_y\phi_\xi^* + \phi_\eta^*) + \frac{\xi_y^2}{\xi_x}(1 + H\xi_x\phi_\xi^*) + H\xi_y(\xi_y\phi_\xi^* + \phi_\eta^*) \tag{8d}$$

$$F_2 = (1/\xi_x)(1 + H\xi_x\phi_\xi^*) \tag{8e}$$

$$F_3 = (1/\xi_x) \tag{8f}$$

$$R = -\xi_x \frac{\Delta t^2}{2A}\left\{ -\frac{A}{\xi_x}\frac{2\phi^* - 5\phi^n + 4\phi^{n-1} - \phi^{n-2}}{\Delta t^2} - B\frac{3\phi_\xi^* - 4\phi_\xi^n + \phi_\xi^{n-1}}{2\Delta t} + \frac{\partial}{\partial\xi}\left[E\xi_x\phi_\xi^* + F\xi_x^2\phi_\xi^{*2} + G(\xi_y\phi_\xi^* + \phi_\eta^*)^2 + \frac{\xi_y}{\xi_x}(\xi_y\phi_\xi^* + \phi_\eta^*) + H\xi_y\phi_\xi^*(\xi_y\phi_\xi^* + \phi_\eta^*)\right] + \frac{\partial}{\partial\eta}\left[\frac{1}{\xi_x}(\xi_y\phi_\xi^* + \phi_\eta^*) + H\phi_\xi^*(\xi_y\phi_\xi^* + \phi_\eta^*)\right] + \frac{\partial}{\partial\zeta}\left(\frac{1}{\xi_x}\phi_\zeta^*\right)\right\} \tag{8g}$$

In Eq. (7), σ is a relaxation parameter which is normally set equal to 1.0. To accelerate convergence to steady state, the residual R may be over-relaxed using $\sigma > 1$. Equation (7) is solved using three sweeps through the grid by sequentially applying the operators L_ξ, L_η, and L_ζ as

$$\xi\text{-sweep:} \quad L_\xi \Delta\bar{\phi} = -\sigma R \tag{9a}$$

$$\eta\text{-sweep:} \quad L_\eta \Delta\bar{\bar{\phi}} = \Delta\bar{\phi} \tag{9b}$$

$$\zeta\text{-sweep:} \quad L_\zeta \Delta\phi = \Delta\bar{\bar{\phi}} \tag{9c}$$

Further details of the algorithm development and solution procedure may be found in Ref. 4.

Engquist-Osher Type-Dependent Switch

An Engquist-Osher (E-O) type-dependent mixed difference operator has been implemented in the AF algorithm to treat supersonic regions of the flow. The E-O switch is based on sonic reference conditions and is applied to both sides of Eq. (7). For example, in the residual [Eq. (8g)] the terms that are upwind biased at supersonic points are defined by

$$\frac{\partial}{\partial\xi}\left(E\xi_x\phi_\xi^* + F\xi_x^2\phi_\xi^{*2}\right) = \vec{\Delta}_\xi \tilde{f}_{i-\frac{1}{2}} + \overleftarrow{\Delta}_\xi \hat{f}_{i-\frac{1}{2}} \tag{10}$$

where

$$\tilde{f}_{i-\frac{1}{2}} = E\tilde{u}_{i-\frac{1}{2}} + F\tilde{u}_{i-\frac{1}{2}}^2 \tag{11a}$$

$$\hat{f}_{i-\frac{1}{2}} = E\hat{u}_{i-\frac{1}{2}} + F\hat{u}_{i-\frac{1}{2}}^2 \tag{11b}$$

$$\vec{\Delta}_\xi \tilde{f}_{i-\frac{1}{2}} = \frac{\tilde{f}_{i+\frac{1}{2}} - \tilde{f}_{i-\frac{1}{2}}}{(\frac{1}{2})(\xi_{i+1} - \xi_{i-1})} \tag{11c}$$

$$\overleftarrow{\Delta}_\xi \hat{f}_{i-\frac{1}{2}} = \frac{\hat{f}_{i-\frac{1}{2}} - \hat{f}_{i-3/2}}{(\frac{1}{2})(\xi_{i+1} - \xi_{i-1})} \tag{11d}$$

$$\tilde{u}_{i-\frac{1}{2}} = \bar{u} + (1 - \epsilon_{i-\frac{1}{2}})(u_{i-\frac{1}{2}}^* - \bar{u}) \tag{11e}$$

$$\hat{u}_{i-\frac{1}{2}} = \bar{u} + \epsilon_{i-\frac{1}{2}}(u_{i-\frac{1}{2}}^* - \bar{u}) \tag{11f}$$

$$u_{i-\frac{1}{2}}^* = \overleftarrow{\delta}_x \phi_i^* = \xi_{x_{i-\frac{1}{2}}} \frac{\phi_i^* - \phi_{i-1}^*}{\xi_i - \xi_{i-1}} \tag{11g}$$

$$\epsilon_{i-\frac{1}{2}} = 1 \quad \text{if} \quad u_{i-\frac{1}{2}}^* > \bar{u} \tag{11h}$$

$$= 0 \quad \text{if} \quad u_{i-\frac{1}{2}}^* \le \bar{u} \tag{11i}$$

In Eqs. (11) the j and k subscripts corresponding to the spanwise and vertical directions, respectively, have been omitted for clarity. Similar differencing is used on the left-hand side of Eq. (7) where the first two terms of F_1 [Eq. (8d)] are upwind biased at supersonic points.

Second-Order-Accurate Spatial Differencing

The AF algorithm with the E-O switch as defined by Eq. (10) is only first-order accurate in supersonic regions of the flow. To achieve second-order accuracy at supersonic and subsonic points, Eq. (10) is extended as

$$\frac{\partial}{\partial\xi}\left(E\xi_x\phi_\xi^* + F\xi_x^2\phi_\xi^{*2}\right) = \vec{\Delta}_\xi \tilde{f}_{i-\frac{1}{2}} + \overleftarrow{\Delta}_\xi \hat{f}_{i-\frac{1}{2}} + \Delta\xi\, \overleftarrow{\delta}_\xi \epsilon_{i-\frac{1}{2}} \overleftarrow{\Delta}_\xi \hat{f}_{i-\frac{1}{2}} \tag{12}$$

Similar modifications to the left-hand side of Eq. (7) result in a pentadiagonal system of equations for subsonic flows with embedded supersonic regions and a tridiagonal system of equations for purely subsonic flows. Furthermore, the treatment of the ϕ_{xt} term in the TSD equation is only first-order accurate in space because of the one-sided differencing used. Similar to Ref. 8, the ϕ_{xt} term is backward differenced to enhance diagonal dominance and, consequently, maintain numerical stability.

Boundary Conditions

Flow Tangency

The flow-tangency boundary conditions are imposed along the mean plane of the respective lifting surfaces, and the wakes are assumed to be planar extensions from the trailing edges to the downstream boundary of the finite-difference grid. The numerical implementation of these conditions[2] allows for coplanar and noncoplanar combinations of horizontal (canard, wing, horizontal tail, launchers) and vertical (pylons, vertical tail) surfaces. Bodies such as the fuselage, stores, and nacelles are treated using simplified boundary conditions on a prismatic surface rather than on the true surface.[2] The method is consistent with the small-disturbance approximation, and treats bodies with sufficient accuracy to obtain the correct global effect on the flowfield without the use of special grids or complicated coordinate transformations.

Far Field

The conditions imposed upon the outer boundary of the computational region are similar to the nonreflecting boundary conditions reported by Whitlow.[9] The conditions employed here are given by

Upstream:

$$\phi = 0 \tag{13a}$$

Downstream:

$$\frac{1}{2}\left(\frac{-B}{C} + \frac{D}{\sqrt{C}}\right)\phi_t + \phi_x = 0 \tag{13b}$$

Above:

$$\frac{D}{2}\phi_t + \phi_z = 0 \tag{13c}$$

Below:

$$\frac{D}{2}\phi_t - \phi_z = 0 \tag{13d}$$

Right spanwise:

$$\frac{D}{2}\phi_t + \phi_y = 0 \tag{13e}$$

Left spanwise (for full-span modeling):

$$\frac{D}{2}\phi_t - \phi_y = 0 \tag{13f}$$

Symmetry plane (for half-span modeling):

$$\phi_y = 0 \tag{13g}$$

where $C = E + 2F\phi_x$ and $D = \sqrt{4A + B^2/C}$. These boundary conditions are numerically imposed by redefining the L_ξ, L_η, and L_ζ operators in Eq. (7) as well as the right-hand side R, at the appropriate grid points. The equation to be solved at boundary grid points may then be written symbolically as

$$\tilde{L}_\xi \tilde{L}_\eta \tilde{L}_\zeta \Delta\phi = -\sigma\tilde{R} \tag{14}$$

where the tilde indicates that the quantity has been rewritten to account for the boundary conditions. For example, along the downstream boundary the three operators and right-hand side are defined as

$$\tilde{L}_\xi = 1 + \frac{4\Delta t}{3}\left(\frac{-B}{C} + \frac{D}{\sqrt{C}}\right)^{-1}\xi_x \frac{\partial}{\partial\xi} \tag{15a}$$

$$\tilde{L}_\eta = 1 \tag{15b}$$

$$\tilde{L}_\zeta = 1 \tag{15c}$$

$$\tilde{R} = \frac{1}{3}\left(3\phi^* - 4\phi^n + \phi^{n-1}\right) + \frac{4\Delta t}{3}\left(\frac{-B}{C} + \frac{D}{\sqrt{C}}\right)^{-1}\xi_x\phi^*_\xi \tag{15d}$$

Time-Linearization Step

An initial estimate of the potentials at time level $(n + 1)$ is required to start the iteration process. This estimate is provided by performing a time-linearization calculation. The equations governing the time-linearization step are derived in a similar fashion as the equations for iteration. The only difference is that the equations are formulated by linearizing about time level n rather than the iterate level (*).

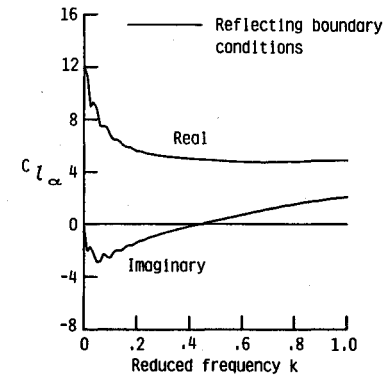

a) Reflecting boundary conditions

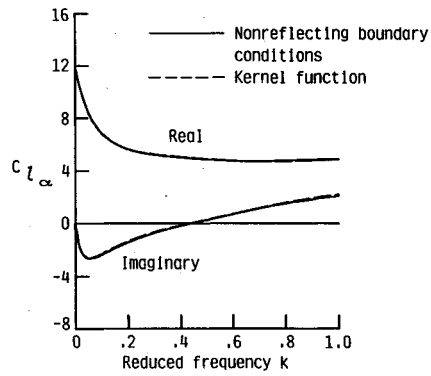

b) Nonreflecting boundary conditions

Fig. 1 Comparisons of unsteady lift-curve slope for a flat plate airfoil at $M = 0.85$.

CAP-TSD Code

The AF algorithm has been used as the basis of the CAP-TSD code for transonic unsteady aerodynamic and aeroelastic analysis of realistic aircraft configurations. The code can treat configurations with arbitrary combinations of lifting surfaces and bodies including canard, wing, tail, control surfaces, tip launchers, pylons, fuselage, stores, and nacelles. The present capability has the option of half-span modeling [Eq. (13g)] for symmetric cases, or full-span modeling [Eq. (13f)] to allow the treatment of antisymmetric mode shapes, fuselage yaw, or unsymmetric configurations such as an oblique wing or unsymmetric wing stores. Steady and unsteady CAP-TSD pressures for several realistic aircraft configurations, including comparisons with experimental data, were presented in Ref. 2. The calculated results were in good agreement with the experimental pressure data, which validated CAP-TSD for multiple component applications with mutual aerodynamic interference effects. Preliminary aeroelastic applications of CAP-TSD compared well with experimental data for subsonic and supersonic freestream Mach numbers, which gives confidence in the code for aeroelastic prediction.[3]

Results and Discussion

Results are presented for several configurations to demonstrate and evaluate the modifications to the AF algorithm of the CAP-TSD code. Calculations are first presented for a flat plate airfoil to assess the effectiveness of the nonreflecting far-field boundary conditions. Calculations are next presented for the F-5 wing[10] and the ONERA M6 wing[11] to demonstrate the improvements due to the Engquist-Osher switch, the second-order-accurate supersonic differencing, and the steady-state convergence acceleration. Finally, steady and unsteady results are presented for the General Dynamics one-ninth scale F-16C aircraft model[12,13] to investigate application of the modified algorithm to a realistic aircraft configuration.

Flat Plate Airfoil Results

Unsteady results were obtained for a flat plate airfoil at $M = 0.85$ to test the nonreflecting far-field boundary conditions. The flat plate airfoil was selected to allow direct comparison of results with the exact kernel function method of Bland.[14] The boundary conditions were tested by computing the lift coefficient due to the airfoil pitching about the quarter chord. Such unsteady forces are typically determined by calculating several cycles of forced harmonic oscillation with the last cycle providing the estimate of the forces. Alternatively, the forces may be obtained indirectly from the response due to a smoothly varying exponentially shaped pulse.[15] In this procedure, the airfoil is given a small prescribed pulse in a given mode of motion (in this case pitching) and the aerodynamic transients calculated. The harmonic response is obtained by a transfer-function analysis using fast Fourier transforms. Use of the pulse transfer-function technique gives considerable detail in the frequency domain with a significant reduction in cost over the alternative method of calculating multiple oscillatory responses. For the flat plate airfoil, pulse transient calculations were performed using 1024 time steps with $\Delta t = 0.2454$. The amplitude of the pulse was 0.5 deg. The grid extended 25 chord lengths above and below the airfoil and 20 chord lengths upstream and downstream of the airfoil. Parallel results were obtained using reflecting (steady-state) and nonreflecting far-field boundary conditions as shown in Fig. 1. The results are plotted as real and imaginary components of the unsteady lift-curve slope c_{l_α} as a function of reduced frequency k. Computations using the reflecting boundary conditions, shown in Fig. 1a, produce oscillations in both the real and imaginary parts for $0 < k < 0.2$. The oscillations are produced by reflected disturbances which propagate back into the near field and contaminate the solution. When the calculation was repeated using the nonreflecting boundary conditions, shown in Fig. 1b, the oscillations no longer occur because the boundary conditions absorb most of the disturbances that are incident on the grid boundaries. Furthermore, these results are in excellent agreement with calculations from the kernel function method of Ref. 14.

F-5 Wing Results

Calculations were next performed for the F-5 wing[10] to assess the algorithm modifications to CAP-TSD. The F-5 wing has an aspect ratio of 3.16, a leading-edge sweep angle of 31.9 deg, and a taper ratio of 0.28. The airfoil section of the wing is a modified NACA 65A004.8 airfoil that has a drooped nose and is symmetric aft of 40% chord. The F-5 calculations were performed using a constant step size for a total of 500 steps. The freestream Mach number was selected as 0.9, and the wing was at 0-deg angle of attack. The results were obtained to study the steady-state convergence characteristics of the modified AF algorithm. The results are presented in the form of convergence histories and the number of supersonic (NSUP) points vs the iteration number.

In the original AF algorithm of Ref. 4, the Murman type-dependent switch was used. Results obtained using the unmodified code are presented in Fig. 2. The steady-state convergence is shown in Fig. 2a; the NSUP, normalized by the final value, are shown in Fig. 2b. For aeroelastic analysis where airloads are required rather than pressures, the solution is considered to be converged to engineering accuracy when a three to four order of magnitude reduction in the solution error is obtained. The "error" in the convergence history, as defined herein, is the ratio of the maximum $|\Delta\phi|$ after n iterations to the maximum $|\Delta\phi|$ in the initial solution (first iteration). Two sets of results are plotted corresponding to two values of step size, $\Delta t = 0.1$ and 0.5. For $\Delta t = 0.1$, the rate of convergence is slow, and the number of supersonic points

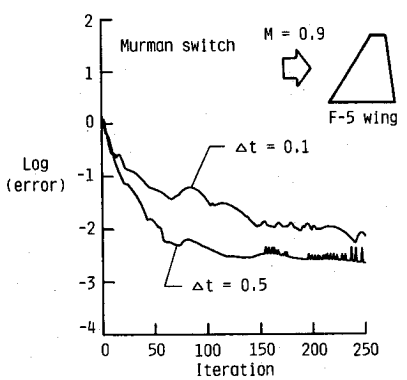

a) Steady-state convergence

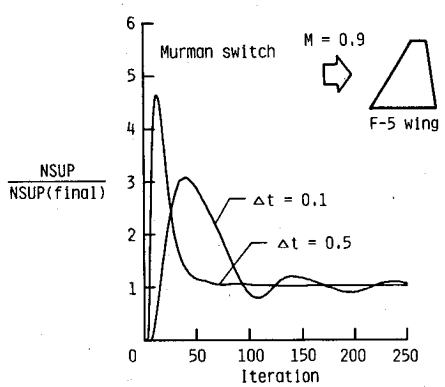

b) Number of supersonic points

Fig. 2 Effects of step size on the solution computed using the Murman switch for the F-5 wing at $M = 0.9$ and $\alpha_0 = 0$ deg.

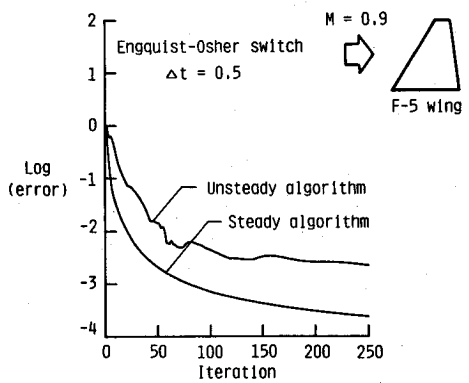

a) Steady-state convergence

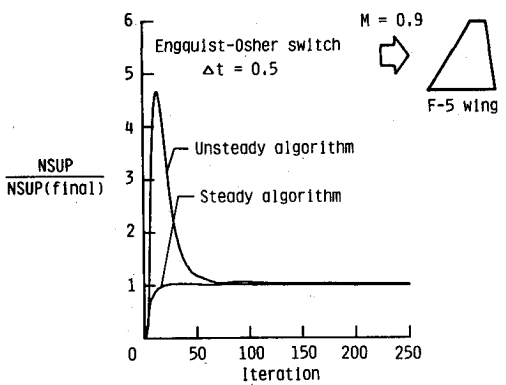

b) Number of supersonic points

Fig. 3 Effects of deleting all TSD time derivatives on the solution computed using the Engquist-Osher switch for the F-5 wing at $M = 0.9$ and $\alpha_0 = 0$ deg.

oscillates about the final value. Increasing the step size to $\Delta t = 0.5$ improves the rate of convergence, and the oscillations in NSUP are significantly damped. The results for $\Delta t = 0.5$ also indicate that the number of supersonic points is initially more than four and one-half times the final value, and that "spikes" begin to appear in the convergence history after 150 steps. These spikes, which represent a numerical instability, are due to a large transient caused by the impulsive start from a uniform stream using a large step size. If the calculations were started with a smaller step size, and then the step size increased to the larger value, the numerical instability can be avoided. Also, as shown in Refs. 2 and 4, the step size may be cycled through very large values such as $\Delta t = 5.0$ to achieve faster convergence to steady state.

The F-5 calculations with $\Delta t = 0.5$ were then repeated with the E-O switch replacing the Murman switch. These results are labeled "unsteady algorithm" in Fig. 3. The curves are almost identical to the $\Delta t = 0.5$ curves of Fig. 2 except that the spikes in the convergence history are absent. The E-O switch is more robust than the Murman switch and, thus, the calculation remains stable. Furthermore, the rate of convergence to steady state could be increased by deleting the time derivatives in the residual, overrelaxing the residual, or deleting all of the time derivatives in the TSD equation.[16] By deleting all of the time derivatives, the algorithm solves the steady TSD equation and is, therefore, referred to as the "steady algorithm." Results obtained using this algorithm are compared with the unsteady algorithm results in Fig. 3. The convergence history computed using the steady algorithm is monotonically decreasing and very smooth in comparison with the unsteady algorithm convergence history. The steady algorithm solution converges faster and does not produce the large initial overprediction of NSUP that is characteristic of the unsteady algorithm. The number of supersonic points converges rapidly to within 2% of its final value in only approximately 25 steps. Overrelaxing the residual of the steady algorithm also further accelerates the convergence to steady state (not shown).

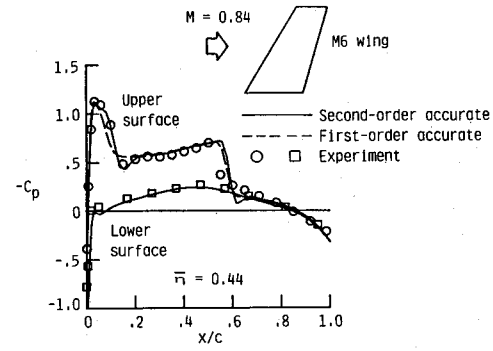

Fig. 4 Effects of first-order and second-order-accurate supersonic differencing on the steady pressure distributions of the ONERA M6 wing at $M = 0.84$ and $\alpha_0 = 3.06$ deg.

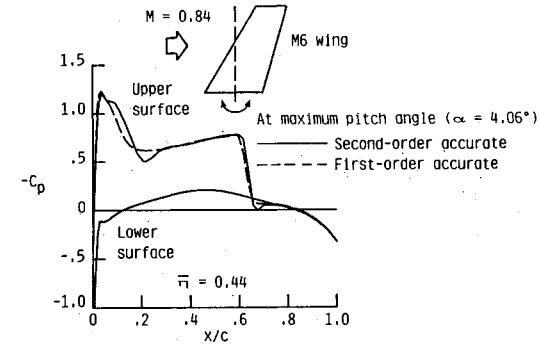

Fig. 5 Effects of first-order and second-order-accurate supersonic differencing on the unsteady pressure distributions of the ONERA M6 wing during the third cycle of rigid pitching at $M = 0.84$, $\alpha_0 = 3.06$ deg, $\alpha_1 = 1.0$ deg, and $k = 0.1$.

ONERA M6 Wing Results

To test the accuracy of the modified CAP-TSD algorithm, calculations were performed for the ONERA M6 wing.[11] The M6 wing has an aspect ratio of 3.8, a leading-edge sweep angle of 30 deg, and a taper ratio of 0.562. The airfoil section of the wing is the ONERA "D" airfoil, which is a 10% maximum thickness-to-chord ratio conventional section. The freestream Mach number was selected as $M = 0.84$, and the wing was at 3.06-deg angle of attack. These conditions were chosen for comparison with the tabulated experimental pressure data of Ref. 11. This rather well-known case is a very challenging one, especially for a TSD code, because of the complex double shock wave that occurs on the upper surface of the wing.

Steady-state calculations were performed for the M6 wing by using the AF algorithm with the E-O switch. The results were obtained by cycling the step size through values as large as $\Delta t = 2.0$ for a total of 500 steps. This relatively large step size corresponds to two root chords of travel per time step. A comparison of the resulting CAP-TSD pressures with the experimental pressure data is given in Fig. 4 for $\bar{\eta} = 0.44$. The data indicate that there is a relatively weak highly swept supersonic-to-supersonic shock wave that forms forward near the leading edge. The primary supersonic-to-subsonic shock that occurs in the midchord region of the wing coalesces with the first shock. Outboard toward the tip, the two shocks merge to form a single supersonic-to-subsonic shock wave. The CAP-TSD results, obtained using first-order-accurate differencing in supersonic regions, are in fairly good agreement with the data in predicting the overall pressure levels, although differences occur in the regions of the shocks. In general, the leading-edge suction peak is well predicted, but the supersonic-to-supersonic shock is smeared. When the calculation was repeated using the second-order-accurate spatial differencing, a significant improvement was obtained in the accuracy of the results. The comparisons in Fig. 4 show that the supersonic-to-supersonic shock is much more sharply captured by the second-order method and, consequently, the calculated pressures are now in very good agreement with the experimental data. The differences that remain between the calculated and experimental pressures near the supersonic-to-subsonic shock may be due to viscous effects or entropy effects, which are presently outside the scope of the present capability. Calculations were also performed for the M6 wing using the original algorithm with the Murman switch. These calculations were unsuccessful because of a numerical instability that was produced by the highly expanded flow about the leading edge of the wing.

An unsteady calculation was also performed for the M6 wing at $M = 0.84$ to investigate the robustness of the modified algorithm for time-dependent applications. In this demonstration calculation, the wing was forced to oscillate in pitch about a line perpendicular to the root at the root midchord. The amplitude of the motion was 2 deg peak-to-peak about the mean angle of attack of $\alpha_0 = 3.06$ deg. The reduced frequency was selected as $k = 0.1$, and only 300 steps per cycle of motion were used. This corresponds to a step size of $\Delta t = 0.1047$. Three cycles of motion were computed to obtain a periodic solution. Unsteady pressure distributions, obtained using first-order and second-order-accurate supersonic differencing, are shown at the maximum pitch angle ($\alpha = 4.06$ deg) in Fig. 5 for $\bar{\eta} = 0.44$. Similar to the steady-state results, these pressure comparisons illustrate that the supersonic-to-supersonic shock is more sharply captured by the second-order method. Further instantaneous pressure distributions at two points during the third cycle of motion are shown in Fig. 6 for five span stations along the wing. Pressures at the wing maximum angle of attack ($\alpha = 4.06$ deg) and pressures at the wing

minimum angle of attack ($\alpha = 2.06$ deg) are both presented in the figure. As the wing pitches up, the shocks move aft, and the supersonic-to-subsonic shock grows in strength. As the wing pitches down, the shocks move forward, and the supersonic-to-supersonic shock is more sharply defined. For this case, both of the shocks oscillate over approximately 10% of the chord during a cycle of motion. Also, the supersonic-to-supersonic shock at $\bar{\eta} = 0.80$ periodically appears and disappears during a cycle of motion. The results illustrate the large shock motions that the modified AF algorithm is capable of computing. The improved algorithm captures the shocks sharply and is sufficiently robust to compute this complex unsteady flow using only 300 steps per cycle of motion.

General Dynamics F-16C Aircraft Model Results

Results were also obtained for the General Dynamics F-16C aircraft model[12] to investigate application of the modified algorithm to a realistic aircraft configuration. Shown in Fig. 7 are the F-16C components that are modeled using CAP-TSD. The F-16C is modeled using four lifting surfaces and two bodies. The lifting surfaces include 1) the wing with leading- and trailing-edge control surfaces, 2) the launcher, 3) a highly swept strake, aft strake, and shelf surface, and 4) the horizontal tail. The bodies include 1) the tip missile and 2) the fuselage. In these calculations, the freestream Mach number was $M = 0.9$, and the F-16C aircraft was at 2.38-deg angle of attack. Also, the leading-edge control surface of the wing was deflected upwards 2 deg for comparison with the experimental steady pressure data of Ref. 13. Furthermore, the calculations were performed on a grid that conforms to the leading and trailing edges of the lifting surfaces and contains 324,000 points. This grid included 160, 27, and 75 points in the streamwise, spanwise, and vertical directions, respectively. Because the grid is Cartesian, it was relatively easy to generate, even for such a complex configuration as the F-16C aircraft. Also, the calculations required only about 0.88 CPU seconds per time step and 13 million words of memory on the CDC VPS-32 computer at NASA Langley Research Center.

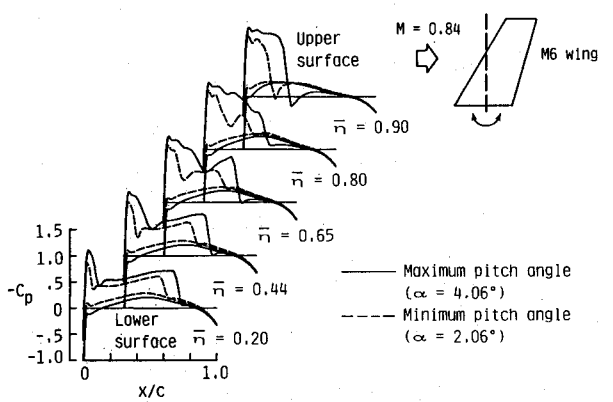

Fig. 6 Instantaneous pressure distributions on the ONERA M6 wing during the third cycle of rigid pitching at $M = 0.84$, $\alpha_0 = 3.06$ deg, $\alpha_1 = 1.0$ deg, and $k = 0.1$.

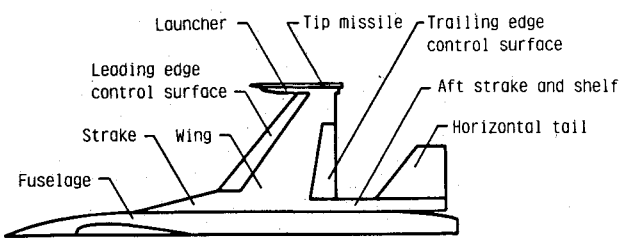

Fig. 7 CAP-TSD modeling of the General Dynamics one-ninth scale F-16C aircraft model.

Steady-state calculations were performed for the F-16C aircraft using the AF algorithm with the E-O and Murman switches. The E-O results were obtained using both the first-order- and second-order-accurate supersonic differencing. Steady pressure comparisons are given in Fig. 8 for three span stations of the wing and one span station of the tail. Both sets of E-O results are presented for comparison with the experimental data. The results obtained using the Murman switch were originally published in Ref. 2. These results are identical to plotting accuracy with the first-order E-O results and, therefore, are not shown. The steady pressure comparisons indicate that there is a moderately strong shock wave on the upper surface of the wing, and the CAP-TSD pressures agree well with the experimental pressures. For the tail, the flow is predominantly subcritical, and the calculated results again agree well with the data. Comparison of pressures computed using first-order- and second-order-accurate supersonic differencing shows very small differences. The largest difference, for example, occurs on the wing at $\bar{\eta}_w = 0.79$ where the second-order calculation predicts a slightly stronger shock.

Unsteady results were also obtained for the F-16C aircraft to investigate the robustness of the modified algorithm for realistic-aircraft time-dependent applications. For simplicity, the calculation was performed for a rigid pitching motion where the entire aircraft was forced to oscillate about the model moment reference axis at a reduced frequency of $k = 0.1$. The oscillation amplitude was chosen as $\alpha_1 = 1.5$ deg, which is three times the value used to obtain similar results presented in Ref. 2. Three cycles of motion were computed using 300 steps per cycle of motion corresponding to $\Delta t = 0.1047$. Calculations were performed using both the Murman and E-O switches. The solution using the original algorithm with the Murman switch, however, was numerically unstable for this case as shown in Fig. 9. Instantaneous pressure distributions at time steps 94 and 95 are plotted in the figure, computed using the Murman (Fig. 9a) and E-O (Fig. 9b) switches. The numerical instability begins in the region of the launcher/tip-missile where the grid spacing is smallest. Figure 9a shows the instability in the form of an oscillation in the wing upper surface pressure distribution at $\bar{\eta}_w = 0.94$ from approximately 30 to 60% chord. The program subsequently failed during step 96, which is 21 steps after the maximum pitch angle in the first cycle of motion. The calculation involving the modified algorithm (E-O switch with the first-order-accurate supersonic differencing) is stable, however, as shown in Fig. 9b. Here, the pressure distributions for steps 94 and 95 are very similar, and the calculation proceeds with no difficulty. In fact, the modified AF algorithm with the E-O switch is numerically stable for this case with either the first-order or second-order supersonic differencing.

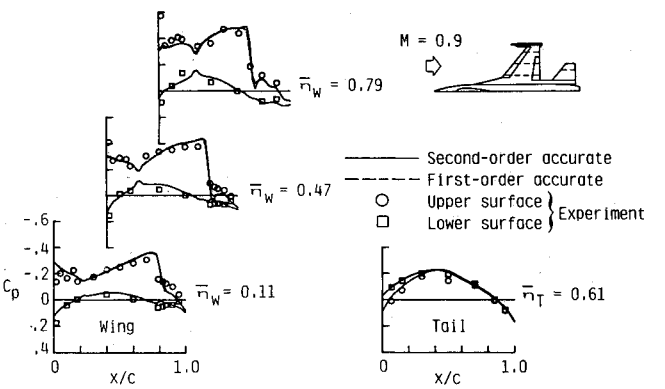

Fig. 8 Comparisons between CAP-TSD steady pressure distributions computed using first-order and second-order-accurate supersonic differencing with the experimental pressure data for the wing and tail of the F-16C aircraft model at $M = 0.9$ and $\alpha_0 = 2.38$ deg.

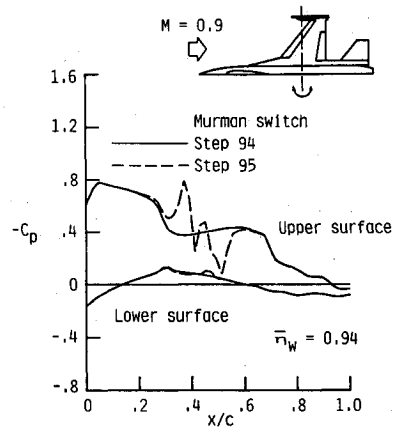

a) Numerical instability with Murman switch

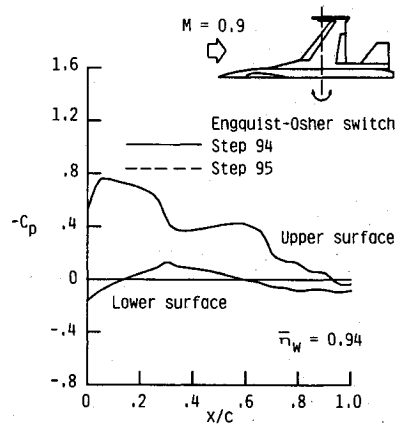

b) Improved numerical stability with Engquist-Osher switch

Fig. 9 Effects of type-dependent switch on numerical stability for rigid pitching of the F-16C aircraft model at $M = 0.9$, $\alpha_0 = 2.38$ deg, $\alpha_1 = 1.50$ deg, and $k = 0.1$.

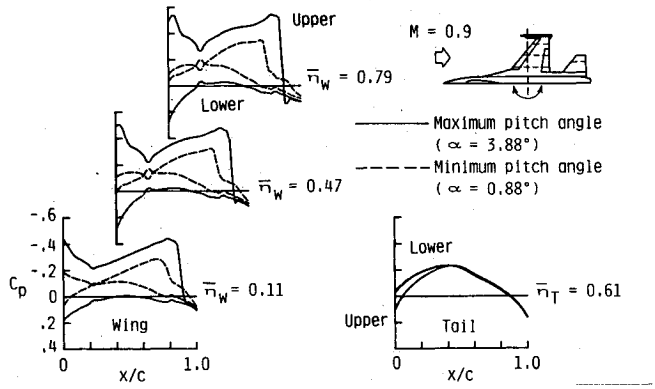

Fig. 10 Instantaneous pressure distributions on the wing and tail of the F-16C aircraft model during the third cycle of rigid pitching at $M = 0.9$, $\alpha_0 = 2.38$ deg, $\alpha_1 = 1.5$ deg, and $k = 0.1$.

Unsteady pressure distributions along the wing and tail during the third cycle of motion are shown in Fig. 10, computed using the E-O switch with the second-order-accurate supersonic differencing. Two sets of calculated pressures are presented corresponding to the aircraft at the maximum ($\alpha = 3.88$ deg) and minimum ($\alpha = 0.88$ deg) pitch angles. Comparison of the results indicates that large changes in pressure occur along the upper and lower surfaces of the wing as the aircraft oscillates in pitch. For example, the shock on the wing upper surface oscillates over more than 10% of the chord during a cycle of motion. Also, the shock is approximately twice as strong at the maximum pitch angle as it is at the minimum pitch angle. For the tail, the changes in the pressure distributions due to aircraft pitching are relatively very small in comparison with the changes in wing pressures, as further shown in Fig. 10. The tail is located considerably aft of the pitch axis and, thus, its motion is plunge dominated, which results in much smaller airloads for the low value of k considered.

Concluding Remarks

Improvements to a time-accurate AF algorithm have been implemented for steady and unsteady transonic analysis of realistic aircraft configurations. These algorithm improvements have been made to the CAP-TSD code developed recently at NASA Langley Research Center. The AF algorithm of the CAP-TSD code solves the unsteady transonic small-disturbance equation. The paper described recent changes to the code that have significantly improved the stability of the AF algorithm and the accuracy of the results. The algorithm modifications include an E-O type-dependent switch to treat regions of supersonic flow, extension of the E-O switch for second-order spatial accuracy, nonreflecting far-field boundary conditions for unsteady applications, and several modifications to accelerate convergence to steady state.

Calculations were presented for the F-5 wing and ONERA M6 wing that demonstrated applications of the algorithm improvements. The results revealed the superior stability characteristics and computational efficiency of the E-O switch. Much larger time steps were possible using the E-O switch, even for comparatively difficult cases. For the particularly challenging case of the M6 wing at $M = 0.84$ and $\alpha_0 = 3.06$ deg, the AF algorithm with the E-O switch was found to be stable for time steps as large as $\Delta t = 2.0$. This relatively large step size corresponds to two root chords of travel per time step. Comparisons of results obtained using first-order and second-order supersonic differencing clearly demonstrated the improved accuracy of the second-order method. Changes to the AF algorithm for convergence acceleration resulted in faster rates of convergence to steady state. Converged solutions were obtained in only several hundred time steps for the F-5 and M6 wings. An unsteady calculation for the M6 wing undergoing a rigid pitching oscillation demonstrated the robustness of the modified AF algorithm. In this calculation, the shocks oscillated over approximately 10% of the chord, and the flow was computed using only 300 steps per cycle of motion. This rather difficult case could not be computed using the original algorithm.

Calculations were also presented for the General Dynamics one-ninth scale F-16C aircraft model to demonstrate application of the modified CAP-TSD code to a realistic aircraft configuration. The F-16C components that were modeled included the wing with leading- and trailing-edge control surfaces, a highly swept strake, aft strake, and shelf surface, the tip launcher and missile, the horizontal tail, and the fuselage. Steady pressure results at $M = 0.9$ and $\alpha_0 = 2.38$ deg compared well with the experimental data. Unsteady results were presented for the entire F-16C aircraft undergoing a rigid pitching motion with a 3-deg peak-to-peak oscillation amplitude. The calculation was a challenging one for the modified algorithm since the flow was computed using only 300 steps per cycle of motion. In this calculation, the shock on the upper surface of the F-16C wing oscillated over more than 10% of the chord, which further demonstrates the robustness of the modified algorithm. Also, similar to the M6 wing example, this case could not have been computed using the original algorithm. Therefore, the modifications have significantly improved the numerical stability of the AF algorithm and the general reliability of the CAP-TSD code for realistic aircraft applications.

References

[1]Edwards, J. W. and Thomas, J. L., "Computational Methods for Unsteady Transonic Flows," AIAA Paper 87-0107, Jan. 1987.

[2]Batina, J. T., Seidel, D. A., Bland, S. R., and Bennett, R. M., "Unsteady Transonic Flow Calculations for Realistic Aircraft Configurations," AIAA Paper 87-0850, April 1987.

[3]Cunningham, H. J., Batina, J. T., and Bennett, R. M., "Modern Wing Flutter Analysis by Computational Fluid Dynamics Methods," ASME Winter Annual Meeting, Boston, MA, Dec. 1987.

[4]Batina, J. T., "An Efficient Algorithm for Solution of the Unsteady Transonic Small-Disturbance Equation," AIAA Paper 87-0109, Jan. 1987.

[5]Murman, E. M., "Analysis of Embedded Shock Waves Calculated by Relaxation Methods," *Proceedings of AIAA Computational Fluid Dynamics Conference,* AIAA, New York, 1973, pp. 27–40.

[6]Engquist, B. E. and Osher, S. J., "Stable and Entropy Satisfying Approximations for Transonic Flow Calculations," *Mathematics of Computation,* Vol. 34, No. 149, Jan. 1980, pp. 45–75.

[7]Goorjian, P. M., Meagher, M. E., and Van Buskirk, R., "Monotone Implicit Algorithms for the Small-Disturbance and Full Potential Equations Applied to Transonic Flows," AIAA Paper 83-0371, Jan. 1983.

[8]Goorjian, P. M. and Van Buskirk, R. D., "Second-Order-Accurate Spatial Differencing for the Transonic Small-Disturbance Equation," *Journal of Aircraft,* Vol. 23, Nov. 1985, pp. 1693–1699.

[9]Whitlow, W., Jr., "Characteristic Boundary Conditions for Three-Dimensional Transonic Unsteady Aerodynamics," NASA TM-86292, Oct. 1984.

[10]Tijdeman, H., Van Nunen, J. W. G., Kraan, A. N., Persoon, A. J., Poestkoke, R., Roos, R., Schippers, P., and Siebert, C. M., "Transonic Wind Tunnel Tests on an Oscillating Wing with External Stores," AFFDL-TR-78-194, Air Force Flight Dynamics Lab., Dayton, OH, Dec. 1978.

[11]Schmitt, V. and Charpin, F., "Pressure Distributions on the ONERA M6 Wing at Transonic Mach Numbers," *Experimental Data Base for Computer Program Assessment,* AGARD-AR-138, Appendix B1, May 1979.

[12]Fox, M. C. and Feldman, C. S., "Model and Test Information Report, 1/9-Scale F-16C and F-16D Force and Loads Model," General Dynamics Rept. 16PR2179, Jan. 1982.

[13]Feldman, C. S., "Wind Tunnel Data Report, 1/9-Scale F-16C Pressure Loads Test," General Dynamics Rept. 16PR2252, July 1982.

[14]Bland, S. R., "Development of Low-Frequency Kernel-Function Aerodynamics for Comparison with Time-Dependent Finite-Difference Methods," NASA TM-83283, May 1982.

[15]Seidel, D. A., Bennett, R. M., and Whitlow, W., Jr., "An Exploratory Study of Finite Difference Grids for Transonic Unsteady Aerodynamics," NASA TM-84583, Dec. 1982.

[16]Batina, J. T., "Unsteady Transonic Algorithm Improvements for Realistic Aircraft Applications," AIAA Paper 88-0105, Jan. 1988.